




Cite this: DOI: 10.1039/d0lc00976h

3-D swimming microdrone powered by acoustic bubbles†

Fang-Wei Liu ^a and Sung Kwon Cho ^{*b}

Received 25th September 2020,
Accepted 25th November 2020

DOI: 10.1039/d0lc00976h

rsc.li/loc

Mobile microrobots that maneuver in liquid environments and navigate inside the human body have drawn a great interest due to their possibility for medical uses serving as an *in vivo* cargo. For this system, the effective self-propelling method, which should be powered wirelessly and controllable in 3-D space, is of paramount importance. This article describes a bubble-powered swimming microdrone that can navigate in 3-D space in a controlled manner. To enable 3-D propulsion with steering capability, air bubbles of three lengths are trapped in microtubes that are embedded and three-dimensionally aligned inside the drone body using two-photon polymerization. These bubbles can generate on-demand 3-D propulsion through microstreaming when they are selectively excited at their individual resonance frequencies that depend on the bubble sizes. In order to equip the drone with highly stable maneuverability, a non-uniform mass distribution of the drone body is carefully designed to spontaneously restore the drone to the upright position from disturbances. A mathematical model of the restoration mechanism is developed to predict the restoration behavior showing a good agreement with the experimental data. The present swimming microdrone potentially lends itself to a robust 3-D maneuverable microscale mobile cargo navigating *in vitro* and *in vivo* for biomedical applications.

Introduction

Underwater, untethered, mobile swimming robots at the microscale have been investigated by many groups due to their potential in serving as a navigating cargo for noninvasive and remote biomedical applications including drug delivery, biosensing, and microsurgery.^{1–7} In order to realize an *in vivo* navigating microrobot, two major issues among many should be addressed: development of (1) efficient self-propulsion at the microscale and (2) maneuverability in 3-D space, that is, control of the propulsion direction as well as the strength. As is well known, the swimming environment and dynamics are characterized by the Reynolds number ($Re = UL/\nu$, where U is the characteristic speed, L the characteristic size and ν the kinematic viscosity of the swimming medium) being interpreted as the ratio of inertia to viscous forces. Since microdrones are on the microscale and move at low speed, propulsion principles should be effective for low Reynolds number environments where the viscous friction is dominant

over inertia. Learning from natural creatures (*e.g.*, bacteria) with cilia or flagella, successful thrusts in such environments generally require asymmetric reciprocating strokes in actuators.^{8,9} When the forward stroke is exactly symmetric to the backward stroke, net propulsion would not be generated under low Re conditions.

Currently existing propelling microengines include using electrical or magnetic fields to drive actuators made of ferromagnetic or paramagnetic materials,^{10–15} harnessing contracting cells, flagellated microorganisms, or bacteria as biohybrid swimmers,^{16–21} utilizing physical or chemical gradients,^{22,23} catalytic reactions,^{24–29} or acoustic excitation,³⁰ *etc.* Although some of them showed promise, they have their own drawbacks. To name a few, the biohybrids driven by microorganisms or cells have difficulty in controlling the direction and magnitude of propulsion. The methods *via* chemical fuels, gradients, or converting energy from light or heat are concerned with their biosafety and accessibility in live organisms. The methods using magnetic or electric fields require bulky and costly equipment to generate strong fields to penetrate into and cover the entire space of navigation.

Acoustic powering that employs resonant oscillation of gaseous bubbles is advantageous for micropropulsion due to the ease of actuation with compact and cost-effective equipment, long sustainability, relatively deep penetration into tissues, and nontoxicity to organisms. The non-zero time-averaged flow induced by an acoustically oscillating bubble, the

^a Department of Mechanical Engineering and Materials Science, University of Pittsburgh, Pittsburgh, PA 15261, USA. E-mail: FAL29@pitt.edu

^b Department of Mechanical Engineering and Materials Science, University of Pittsburgh, Pittsburgh, PA 15261, USA. E-mail: skcho@pitt.edu

† Electronic supplementary information (ESI) available: 13 movie clips are provided to enhance the understanding. See DOI: 10.1039/d0lc00976h

so-called microstreaming, has been used to generate propulsion at microscale. One of the effective configurations to generate microstreaming is to oscillate a gaseous bubble trapped in a one-end open microtube (Fig. 1a).³¹ The gas-liquid interface near the opening of the tube moves back and forth at high frequency (\sim kHz or higher) of the acoustic excitation and generates a non-zero time-averaged net flow, microstreaming flow. Here, the Reynolds number based on the high-frequency oscillating speed is not low anymore unlike the low-frequency swimming strokes in bacteria. This means that the inertia effects play a role in generating the non-zero time-averaged flow, which in turn acts as a reaction force on the tube. This reaction force eventually propels the tube in the opposite to the microstreaming flow direction.

Using this concept, microswimming along the 1-D path was demonstrated.^{32,33} Moreover, the cylindrical bubble trapped in the tube has its own resonance frequency at which the generated propulsion force becomes maximum.³⁴ The resonance frequency critically depends on the length of the bubble for a given system. This implies that the frequency becomes a key control parameter for which bubbles are selected to turn on and off out of a group of bubbles with different lengths.^{35,36} Capitalizing on these characteristics, microswimmers with 2-D steering have been developed. The 2-D steering was achieved by embedding and orthogonally aligning two groups of microtubes differentiated by the bubble length (Fig. 1b).^{35,37} Each of them could be selectively resonated and energized by activating at its resonance frequency while the other group is suppressed in oscillation.

However, all these propelling and steering motions were limited to the 2-D solid plane. Recently, there have been attempts to generate microswimming in a 3-D space using microstreaming. Louf *et al.* used combined actuation forces:

(1) microstreaming to repel a microswimmer made of a half-capsule shell from the solid ground and (2) acoustic radiation forces to move it laterally.³⁸ Another approach is to use a magnetic force to assist steering in a 3-D space. Ren *et al.* introduced a magnetic force to tilt a microswimmer partially coated with a magnetic material such that the secondary Bjerknes force becomes effective in attracting the microswimmer to a solid boundary.³⁹ As a result, the microstreaming and secondary Bjerknes force jointly generated a unidirectional force in a 3-D space. This configuration was later simplified by introducing a fin to re-direct the microstreaming flow and adjust the orientation of the microswimmer to generate the secondary Bjerknes force.⁴⁰

This article describes a 3-D maneuverable microdrone, solely powered and directed by microstreaming, which incorporates two unique designs: (1) 3-D arrangement of microtubes (bubbles) to generate independent thrusts in 3 different directions; (2) non-uniform mass distribution in the drone body to restore the drone to the upright posture and enhance stability in control.⁴¹ Propelling the drone and reaching any position in a 3-D space by microstreaming require multiple propulsion forces: for example, upward/downward in the vertical direction and clockwise/counterclockwise in yaw. In the present design, one group of microtubes is to generate the upward propulsion while the downward motion is driven by gravity (Fig. 1c). Two more groups of tubes generate clockwise/counterclockwise yaws, respectively. This necessity brings extremely high complexity to the structure and fabrication of the swimming microdrone. This challenging issue is overcome by using a 3-D printing method. A 3-D swimming microdrone with all these 3-D aligned microtubes was made within a volume less than 1 mm³ using a two-photon polymerization 3-D printer.

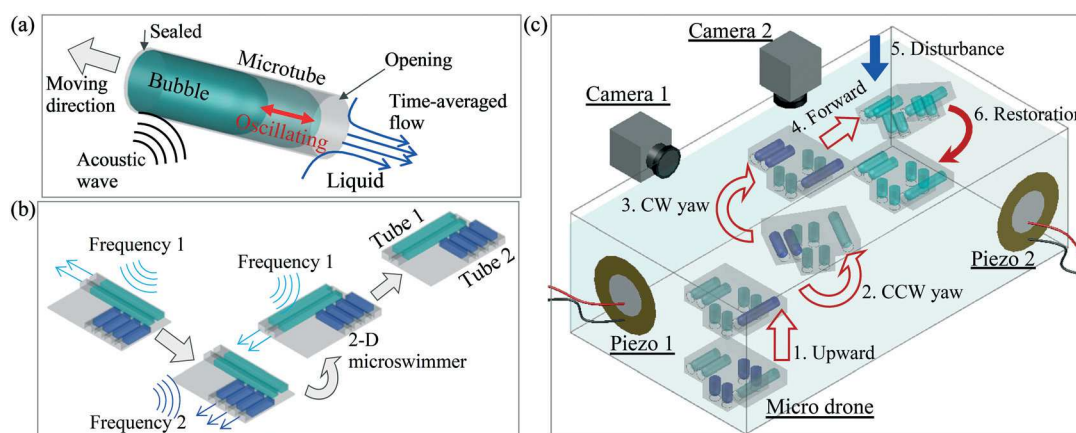


Fig. 1 (a) The non-zero time-averaged microstreaming flow generated by the acoustically oscillating gaseous bubble propels the microtube submerged in a liquid environment. (b) The 2-D microswimmer steers on a solid surface by two groups of microbubbles with different lengths: long bubbles (light blue) and short bubbles (dark blue). Each of the groups is selected and excited when the acoustic frequency matches its resonance frequency that highly depends on the bubble length. (c) The schematic and testing setup of the 3-D swimming microdrone powered by three different types of microbubbles, which selectively generate propulsion forces in three directions. The bubbles trapped in the tubes can be resonantly oscillated by an external acoustic wave via the piezo-actuators. The resonated bubbles (highlighted in dark blue) generate propulsion. Note that the frequency of the acoustic wave determines which bubbles are activated. The microdrone has the capability to restore to its orientation by careful design of its mass distribution.

In the meantime, controlling propulsion in 3-D is also highly challenging. For swimming on a 2-D surface, the solid surface on which a microswimmer sits serves as a constraint to allow the microswimmer to stay on it all the time. For swimming in a 3-D space, however, the number of spatial variables increases, and thus the control of the swimming drone becomes more difficult; any external disturbances or actuations agitate the drone in a random orientation and make subsequent actuations unpredictable. It is critically necessary for the drone to automatically restore to a pre-determined posture regardless of disturbances or prior actuations. This function is achieved by re-distributing the mass in the drone body. Mismatching between the centers of mass and buoyancy always generates a restoring torque to bring the drone to the upright posture. These two unique designs facilitate highly maneuverable swimming in 3-D space, bringing the present swimming microdrone much closer to practical applications.

Results

First and second generation design of the microdrone

In order to reach any place in 3-D space, the first requisite is to generate independent thrusts in three directions. The 1st generation design of the drone has three groups of microtubes assigned for upward (270 μm long) and lateral (560 and 1300 μm long) thrusts, respectively (Fig. 2a). Note that the downward motion is produced by gravity since the overall density of the drone is higher than that of the surrounding fluid. In more detail, the 8 vertically aligned microtubes (270 μm long) have the opening facing downward to generate propulsion in the positive z -direction, the two 1300 μm long microtubes are placed on an x - y plane to produce linear propulsion in the y -direction, and the four 560 μm microtubes are located in the center region of the drone to generate a thrust in the x -direction.

First, the fabricated drone is tested (Fig. 2b; Video S1, ESI†). Initially in the absence of acoustic excitation, the drone takes an equilibrium state where the left side of the drone is slightly lower than the right side and the openings of the 270 μm microtubes face upward (first photo in Fig. 2b). This is due to the fact that the drone has more mass in the upper part. As soon as an acoustic input is given at 13.3 kHz and 5.5 volts, the 270 μm long microtubes are activated and push the drone downward against the bottom. Eventually, the drone is swimming away in a random direction and becomes uncontrollable (second and third photos in Fig. 2b).

This experiment reveals that the gravity and buoyancy forces are significantly influential to the dynamics of the drone at the present size. Learning from this unsuccessful yet instructive result, the 2nd generation drone has been designed to investigate the dynamics and stability associated with gravity and buoyancy (Fig. 2c). Overall, the microdrone has similar dimensions in the main body and microtubes to the first generation drone. The main modification is that all the microtubes are located in the top half of the drone body. As a result, the density of the upper part of the drone is lower than that of the lower part. In order to examine the stability of the drone, the drone initially oriented in a random orientation is released without any acoustic actuation from a position several millimeters above the bottom solid surface (Fig. 2d; Video S2, ESI†). As the drone falls freely down to the solid surface by gravity, it automatically rotates and finally lands on the surface in the upright posture. The redistribution of microtubes generates a righting moment (restoring torque) to recover the drone to the upright position. The more detailed mechanism on this restoration is studied in the following section.

Mechanism of rotation

The above result shows that the distribution of the microtubes and mass significantly affects the balanced

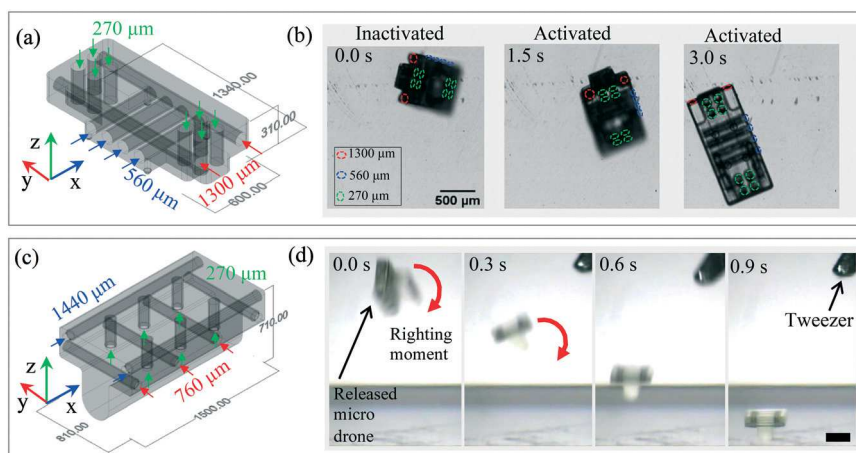


Fig. 2 (a) 1st generation design of the microdrone: the microdrone having microtubes distributed over the entire body and (b) its resting state and activated state by an external acoustic wave in water. The propelling motion is uncontrollable. (c) 2nd generation design of the microdrone: the microtubes are deliberately placed in the upper part of the body. (d) The drone automatically restores to the upright posture after being released in an initially random orientation.

position and dynamics of the drone in the present sub-millimeter size. Re-distributing the microtubes in the drone body effectively relocates the center of mass. The key idea to generate a righting moment (restoring torque) is to have the center of gravity (CG) mismatched with the center of buoyancy (CB): the CG is below the CB by δ (Fig. 3a).^{42,43} The microtubes filled with air bubbles are deliberately located in the upper part of the drone. As a result, the density of the upper part of the drone is lower than that of the lower part since the density of the gas-filled microtube is much lower than that of the solid drone body itself. Consequently, the CG is located below the CB. Note that the location of the CB is determined by the outline of the drone regardless of how microtubes are located inside the drone. Whenever disturbances or acoustic actuation forces deviate the drone from the upright posture by θ or $-\theta$ (Fig. 3b and d), the mismatch between the CG and CB generates a restoring torque to bring the drone back to the upright position where the net torque acting on the drone is zero.

The restoration mechanism and dynamics based on this configuration can be formulated by the balance of torque on the drone about its center of gravity (CG):

$$I \frac{d^2\theta}{dt^2} + A\mu R^3 \frac{d\theta}{dt} + \rho V g \delta \sin\theta = 0, \quad (1)$$

where I is the moment of inertia of rolling or pitching, θ the angular displacement, A the rotating drag coefficient, μ the dynamic viscosity of the surrounding fluid, ρ the density of the surrounding fluid, R the equivalent drone radius based on the drone volume V , g the gravity (9.8 m s^{-2}) and δ the distance between the CB and CG. The first, second and third terms in eqn (1) represent the angular momentum change, the viscous torque by friction, and the torque by the buoyancy force with the lever arm δ , respectively. The viscous torque for a sphere can be expressed as $8\pi\mu R^3 \frac{d\theta}{dt}$.⁴⁴ In eqn (1), coefficient A is introduced to accommodate the geometry deviation of the drone from the sphere and later experimentally determined by curve-fitting the restoration process in the time domain. The behavior described by eqn (1) is an overdamped second order system, and can be analogous to the classic mass-spring-damper system where the time constant is obtained with an approximation of $\sin\theta \approx \theta$ as:⁴⁵

$$\tau = \frac{2I}{A\mu R^3 - \sqrt{(A\mu R^3)^2 - 4I\rho V g \delta}} \quad (2)$$

At $t = \tau$, the overdamped system reaches $\sim 63\%$ of its equilibrium state; at $t = 4\tau$, $\sim 98\%$. Thus, 4τ can be used as a time measure for the drone to complete its restoration process. Eqn (2) provides critical information on how to design a drone, how long the acoustic signal turns on and off, and how the drone behaves dynamically.

Third generation design of the microdrone

The above 2nd generation drone cannot generate any controlled yaw motion: all the 2 lateral tubes for the x -direction propulsion have the same length and so do all the 4 lateral tubes for the y -direction propulsion. In addition, in the 2nd generation design, the shortest tubes were used for the z -direction propulsion. However, experiments show that longer tubes generally produce stronger propulsion. Since the drone naturally sinks under no actuation, the z -direction needs the strongest propulsion, that is, requiring longer tubes. Based on the experiences from the 1st and 2nd generation designs of the drone, stability analyses, and experimental trials, a few modifications from the 2nd generation design are made to improve the stability and maneuverability and eventually lead to the 3rd generation design (Fig. 4).

The more detailed features of the 3rd generation microdrone are described below. The 3rd generation drone can steer on the x - y plane and change the elevation in the z -direction. Three types of microtubes are placed in different orientations and positions inside the drone body. The length and the number of each type are as follows: “lateral 1” ($890 \mu\text{m}$ long \times 2), “lateral 2” ($590 \mu\text{m}$ long \times 3), and “vertical” ($470 \mu\text{m}$ long \times 6). In previous studies,^{33,37} the direction of propulsion is generally opposite to the side of the microtube opening, although some exceptional cases were rarely observed under particular conditions.⁴⁶ The tube lengths of lateral 1 and 2 are different such that they can generate clockwise as well as counterclockwise yaw motions and y -direction propulsion. Lateral 1 lying parallel to the right rooftop plane of the microdrone generates a counterclockwise yaw; in contrast, lateral 2 generates a

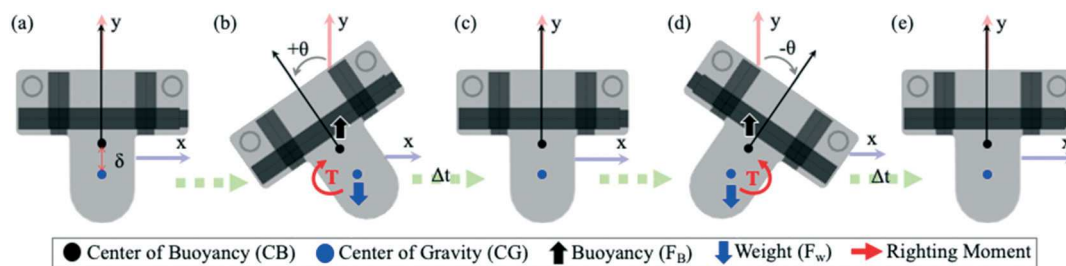


Fig. 3 Restoring mechanism: non-uniform mass distribution restores the drone to the upright position. (a) The location mismatch between the CB and CG generates a restoring torque (T) when the drone is tilted. (b) and (c) show restoration from a counterclockwise tilting while (d) and (e) show restoration from a clockwise tilting.

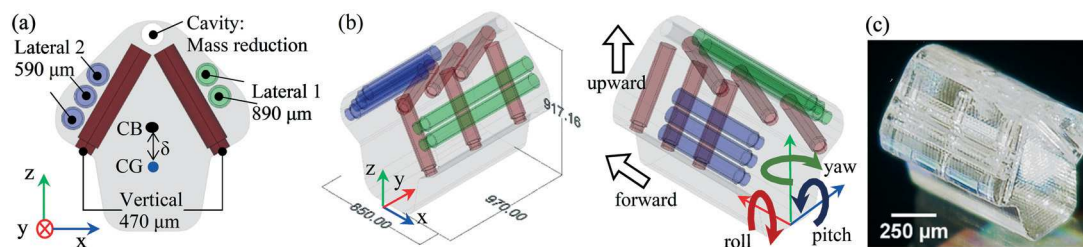


Fig. 4 3rd generation design of the microdrone with three groups of microtubes: (a) the front view and (b) bird's eye view. (c) The photo of the fabricated 3-D microdrone taken using a 3-D digital microscope (HIROX, USA).

clockwise yaw. When both lateral 1 and 2 are activated at an equal thrust, the drone propels straight forward in the positive y -direction. The overall shape (like a thick arrow) of the 3rd generation drone has more mass in the lower body for effective restoration. It creates a larger distance between the CB and CG for restoration. In addition, the tilted rooftop can more easily accommodate longer tubes to generate a stronger upward thrust overcoming the gravitational sinking. The six tilted microtubes (vertical) parallel to the rooftop are designed to propel the microdrone upward. Here, the locations of the vertical tubes are carefully selected to compensate unbalanced mass between the sides of lateral 1 and 2 caused by the different lengths of the lateral 1 and 2 tubes. Note that the openings of the vertical tubes are placed in a distance above the bottom of the drone, which facilitates stable take-off and landing from/to the ground. Otherwise, the microstreaming flow near the opening is interfered with the ground surface making propulsion more unstable.

Another unique feature in this design is to incorporate a sudden contraction near the opening of each tube. The diameter of the microtubes is reduced from $100\ \mu\text{m}$ to $80\ \mu\text{m}$ at the inner positions of 30, 50 and $70\ \mu\text{m}$ from the openings for vertical, lateral 2 and lateral 1, respectively. When a dried swimming drone is immersed in liquid (water or water-glycerol mixture) to trap a bubble in each tube, the water-air interface is pinned at the contraction due to the re-direction of surface tension.⁴⁶ As a result, such contractions allow for uniform and consistent bubble lengths in every experiment.

When all tubes are inactive, the drone spontaneously moves downward in DI water by gravity since the overall

density ($1048\ \text{kg m}^{-3}$) of the drone is higher than that of the DI water ($999\ \text{kg m}^{-3}$). The addition of glycerol increases the density of the liquid and thus minimizes any natural downward motion by gravity. This addition is done only where experiments need to demonstrate the pure effect of propulsion by the lateral 1 and 2 tubes. Moreover, note that the viscosity of the water-glycerol mixture (5:1 ratio, $1.53 \times 10^{-3}\ \text{Pa s}$) is closer to that of the blood plasma ($1.8 \times 10^{-3}\ \text{Pa s}$) than DI water ($0.9 \times 10^{-3}\ \text{Pa s}$). In addition, a dummy cylindrical void (cavity) with both ends open in the roof corner is additionally introduced to reduce and re-distribute the mass in the upper part of the drone, as discussed in the previous section. In this design, the CG is $22\ \mu\text{m}$ below the CB along the gravitational line in the upright posture. The resultant density of the drone above the CB is $951\ \text{kg m}^{-3}$ while the one below is $1138\ \text{kg m}^{-3}$.

The experimental confirmation of the present drone restoring mechanism is shown in Fig. 5a and b (Videos S3 and S4, ESI†). As soon as the microdrone initially held by tweezers in random orientations is released, the drone experiences free fall by gravity and is rolled or pitched back to the upright position. The rolling moment of inertia (I_r) is $4.25 \times 10^{-17}\ \text{kg m}^2$, and the pitching moment (I_p) of inertia is $6.58 \times 10^{-17}\ \text{kg m}^2$, the liquid viscosity μ ranges from 0.9 to $1.5\ \text{Pa s}$, the fluid liquid density ρ ranges from 999 to $1045.4\ \text{kg m}^{-3}$ depending on the mixing ratio between DI water and glycerol, the equivalent drone radius R derived from the drone volume is $456\ \mu\text{m}$, the drone volume V is $4.9 \times 10^{-10}\ \text{m}^3$, and the distance between the CB and CG δ is $22\ \mu\text{m}$. Using the present drone, the restoring history for rolling is

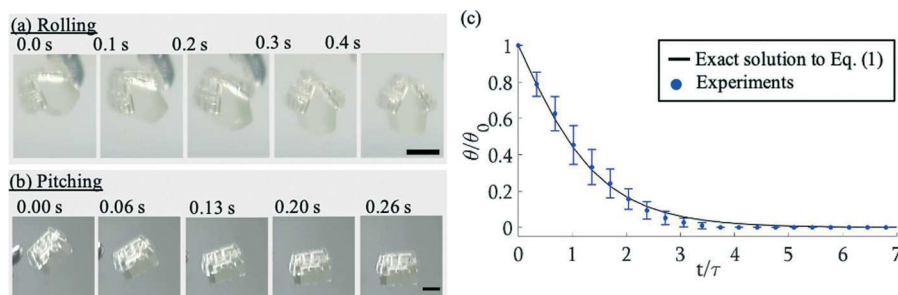


Fig. 5 Restoring results: immediately after the drone in a random orientation is released. It completely restores to the upright position within 0.4 s by (a) rolling and (b) pitching. (c) Restoring behavior in rolling in the time domain; the averaged data of 21 trials are compared with the solution to eqn (1). Time constant τ is estimated to be about 0.1 s (all scale bars: $500\ \mu\text{m}$).

measured in the time domain. As shown in Fig. 5c, the measured data in the rolling angle, the average of 21 experimental trials, are plotted along with the exact solution to eqn (1), where the dimensionless angular displacement θ/θ_0 and the dimensionless time t/τ are used. Overall, they are in excellent agreement. Using these data, coefficient A in eqn (1) is determined to be 76.6 which is about 3 times larger than 25.1 of spherical objects, and the time constant τ of restoration is calculated to be 0.1 s for this design. Due to the dominant viscous friction, the restoring process shows an overdamped behavior. Within 4τ or 0.4 s, the restoring process is 98% completed, meaning that as far as the pause interval between consecutive actuations is maintained to be 0.4 s or longer, the position of the drone is readily upright before the next actuation starts. Based on this result, a pause longer than 0.4 s is added to the actuation signal.

3-D maneuverability. To examine the performance of the individual groups of microtubes, each type of tube was solely activated by its resonance frequency. The vertical microtubes can be excited at 11.7 kHz, and propel the microdrone upward: either taking off from the bottom of the tank or moving up from a suspended position. In DI water, the inactive microdrone sits at the bottom of the tank due to gravity. By applying 58 V to the piezo-actuator as shown in Fig. 6a (Video S5, ESI†), the drone takes off and moves upward. In the water-glycerol mixture, the inactive microdrone can suspend anywhere in the solution and move

upward from the location by applying 24 V to the piezo-actuator (Fig. 6b, Video S6, ESI†) in a 3-D space. The upward speed can reach almost 4 mm s^{-1} . The efficacy of the pause signal (a pause of 0.57 s between consecutive actuations of 0.43 s) is clearly captured in Fig. 6a while the microdrone propels upward. The microdrone tilts slightly backward in the pitching angle (snapshots at 0.5, 1.5, and 2.5 s) while the thrust is on. The above tilting is mainly attributed to the asymmetric arrangement of the vertical tubes. During the pauses after each actuation, the microdrone returns to its upright position, as shown in the snapshots at 1.0, 2.0, and 3.0 s. The activation signal for vertical slightly affects lateral 1 and lateral 2, thus generating a non-negligible propulsion force by lateral 1 and lateral 2. Although each type of microtube is designed to dominantly oscillate at its own resonance frequency, it can still oscillate at the off-resonance frequencies with a low magnitude and generate non-negligible propulsion forces in some cases. However, this crosstalk is barely observed when vertical is activated with voltages below 48 V that are still high enough to elevate the drone from a suspended state (Fig. 6b).

Yawing is tested on the microdrone suspended in the water-glycerol mixture, where friction from the bottom solid surface is excluded. The lateral 1 microtubes are activated at 5.9 kHz and 22 V and yaw the microdrone counterclockwise (Fig. 6c; Video S7, ESI†), while the lateral 2 microtubes yaw the microdrone clockwise when excited at 7.9 kHz, 29 V

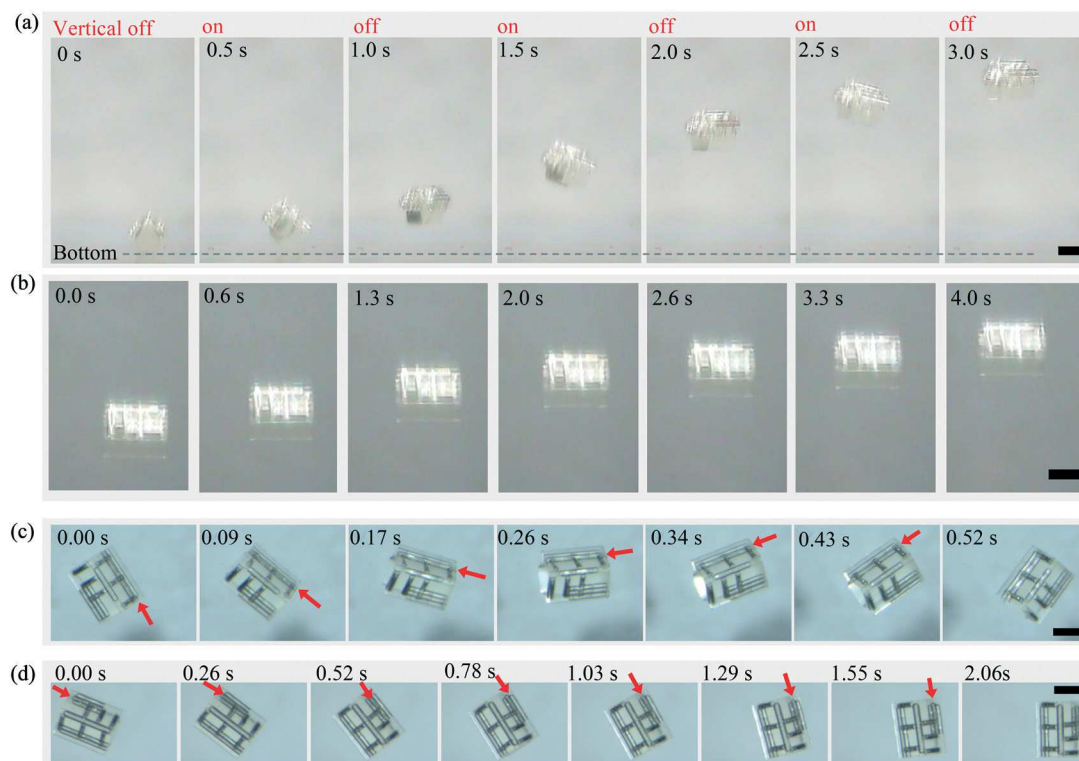


Fig. 6 Activations of individual tube types: (a) vertical for propelling upward from the bottom, (b) vertical for propelling upward from suspension, (c) lateral 2 for clockwise yawing, and (d) lateral 1 for counterclockwise yawing. The red arrows show the locations of the activated microtubes and their direction of propulsion (all scale bars are 500 μm).

(Fig. 6d; Video S8, ESI†). These results confirm that each type of microtube can be independently and selectively activated by changing the activation frequency.

Consecutive and joint activations of multiple microtubes can generate a variety of propelling paths for the drone, demonstrating successful maneuverability (Fig. 7). Path 1 consists of consecutive actuations of lateral 2 followed by vertical conducted in DI water (Fig. 7a; Videos S9 and S10, ESI†). First, the microdrone yaws clockwise due to the propulsion from lateral 2 and simultaneously sinks due to gravity. Then, the drone stops yawing as soon as lateral 2 is deactivated. Next, as vertical is activated, the drone moves upward against gravity. During this movement, a slight quivering of the drone can be observed. This is due to the internal noises from the instruments that occur when switching to a different frequency at relatively high voltages.

For a clearer demonstration, path 2 (Fig. 7b; Video S11, ESI†) is conducted in a water-glycerol mixture that has a similar density to that of the drone to eliminate the downward motion by gravity. Path 2 consists of two cycles

of the activation of vertical followed by the joint activation of lateral 1 and lateral 2. In the first cycle, the microdrone sits at the bottom of the tank, lifts up when vertical is on, and then moves forward (left) when both lateral 1 and 2 are on at an equal thrust (snapshots on the first row in Fig. 7b). Note that due to unequal thrusts, acoustic streaming of the surrounding liquid or background stream, the drone drifts right while moving up. After all activations stop, the microdrone loses its propulsion and suspends in the medium. Then, the same actuation procedure is conducted in cycle 2. The microdrone moves upward and then forward (left) again from the starting position.

Path 3 is accomplished by joint activations of all types of microtubes at the same time in the water-glycerol mixture. The microdrone propels upward and forward simultaneously (Fig. 7c; Videos S12 and S13, ESI†). Based on all the results above, the swimming microdrone has the capability to reach any place in 3-D space by moving upward, downward, and forward and yawing clockwise and counterclockwise.

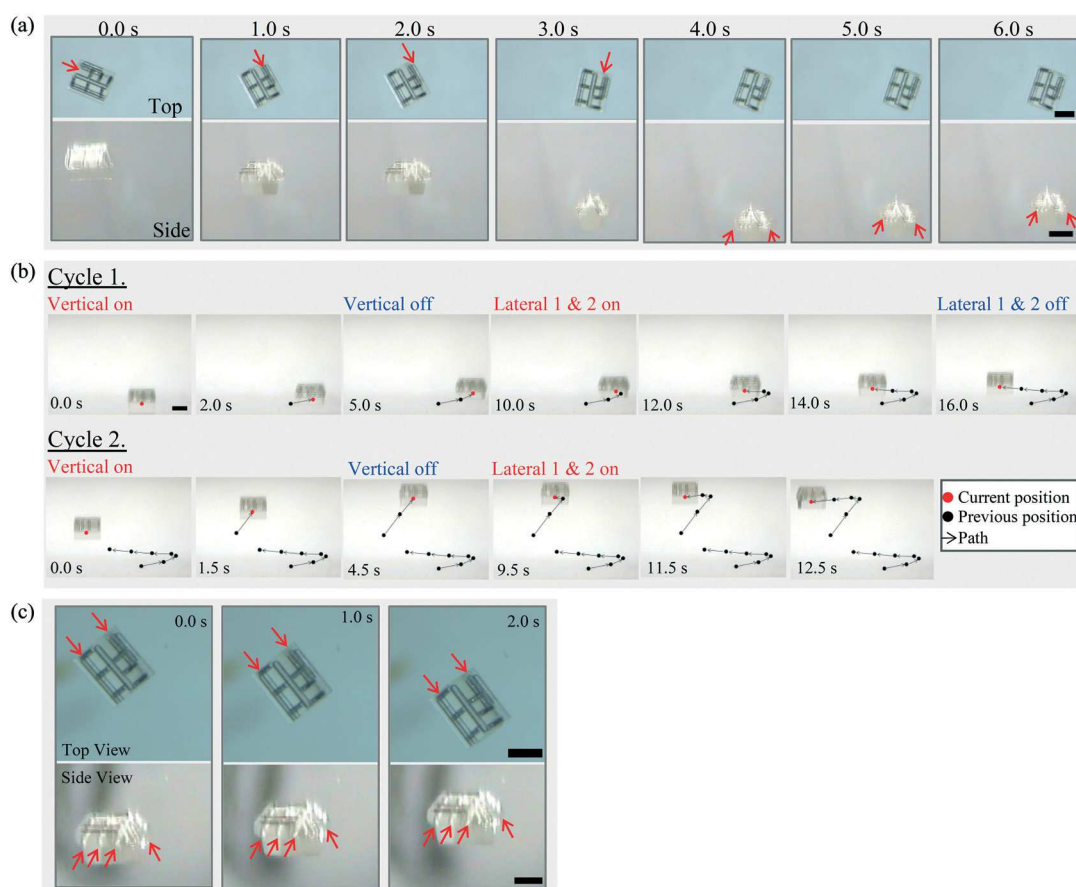


Fig. 7 (a) Consecutive actuations (the top and side views are recorded simultaneously). Activation of lateral 2 resulting in turning counterclockwise but sinking due to gravity. Activating the vertical tubes elevates the drone upward. (b) Consecutive and joint actuations. Cycle 1: the drone first rests on the bottom surface, then takes off by activation of the vertical tubes, and moves left by activation of the lateral 1 & 2 tubes. After all activations stop, the same procedure is conducted again and generates a similar motion in cycle 2. The red dots indicate the center of the drone; the black dots indicate the previous positions; the black arrows show the overall trajectory from 0.0 s. (c) Simultaneous activation of all the tubes results in moving straight forward and upward (against gravity). The red arrows point the locations of the activated microtubes and resultant directions of propulsion (all scale bars are 500 μm).

Discussion

The current design of the swimming microdrone can provide a solution for remotely controlled underwater microvehicles in the size of sub-millimeter range. The 3-D printing technique can reach the resolution of 200–300 nanometers, which is believed to allow the fabrication of microdrones down to tens of microns in the overall size. In this scale, the Brownian motion of the drone is expected to be not significant. The major challenges in the scaling down of the current swimmer include the efficacy of the restoration mechanism and the lifetime of the microbubbles. The performance of the drone may be limited by the prolonged restoration time as the size becomes smaller. The approximated time constant of restoration in eqn (2) is proportional to $1/\sqrt{V\delta}$, which can roughly scale with $1/R^2$. For example, a drone of 100 μm in size would have a restoration time of about 40 s compared to 0.4 s of the microdrone of ~ 1 mm in size. This may be impractical in some applications. In the present state, we expect that the drone performs effectively in the range of hundred microns to millimeters in the overall size.

As the bubble size becomes smaller, the acoustic frequency should increase; higher frequency ultrasound inputs should be used. Another issue in the smaller scale is the lifetime of gaseous bubbles. The gas in bubbles dissolves faster due to the high surface-area-to-volume ratio, resulting in a shorter lifetime. However, the lifetime of bubbles can be significantly extended by the encapsulation of bubbles with a lipid layer and/or using insoluble gas,^{47,48} which is commonly applied to clinically used ultrasound imaging contrast agent microbubbles. In addition, in the present study, trapping the bubbles inside the microtube delays the dissolution of air to the liquid and thus increases the lifetime. Moreover, the bottle neck design (contraction near the tube opening) can improve the bubble stability during oscillation and prevent any bubbles from escaping out of the tube. Experiments showed that the bubbles in the tube can operate for 2–3 hours under intermittent actuations with no significant impact on the overall propulsion, restoration behaviors and controllability. This period would be adequate for many applications.

The propulsion strength by microbubbles depends on their length as well as the response of associated components to the acoustic excitation including the piezo-actuators, amplifier, tank, *etc.* In addition, the resultant oscillating amplitudes of microbubbles vary from one location to another due to the reflection and dissipation of acoustic waves during propagation. This issue may be resolved by using focused beams that are uniformly exposed only to the drone and its limited surrounding area but not the entire field.

Conclusions

This article presents a swimming microdrone navigating in a 3-D space in a controlled manner, which may serve as a cargo to deliver drugs, to sense biosignals and to perform

microsurgeries in the hard-to-reach areas inside the human body. The drone is propelled by microstreaming flows that are generated by acoustically oscillating cylindrical bubbles. The present drone has two unique features. One is that it can be propelled in multiple directions in a controlled manner. This is realized by using multiple bubbles (tubes) of different lengths that are three-dimensionally embedded in the drone. By switching the acoustic frequencies, only resonance-frequency matched bubbles are selectively activated and generate propulsion. As a result, the drone is propelled upward or forward, and yawed clockwise or counterclockwise in an on-command manner. The downward motion is generated by gravity. By individually or jointly using these motions, the swimming microdrone is able to reach any position in a 3-D space.

The other feature is that the careful design of mass distribution in the drone body significantly enhances the stability of the drone. Otherwise, the drone easily loses its orientation by any external disturbances or actuations making it extremely difficult to properly program subsequent actuations to reach the destination. The mismatch between the centers of gravity and buoyancy due to the non-uniform mass distribution generates a restoring torque to return the drone back to the upright posture all the time. This critically facilitates determining the subsequent actuation sequences and thus following a pre-determined navigating path. In addition, the mechanism of this restoration is mathematically analyzed and evaluated with experiments, showing an excellent agreement. Utilizing these features, a variety of programmed swimming paths are experimentally achieved, demonstrating the 3-D maneuverability of the swimming microdrone.

Experimental

Fabrication of the swimming microdrone

The swimming microdrone was fabricated using a Nanoscribe Photonic Professional system (Nanoscribe GmbH, Germany), a 3D laser printer utilizing two-photon polymerization. The laser beam cures the target photoresist (IP-S, Nanoscribe GmbH, Germany) on an ITO (indium tin oxide)-coated substrate into the designed structure at the micrometer scale. The configuration type is the DiLL large scale. The laser power and scanning speed are 80 mW and 90 mm s⁻¹ for the shell, and 90 mW and 100 mm s⁻¹ for the scaffold, respectively. Afterwards, the excess photoresist was removed by SU8-developer (MicroChem Corp., USA) followed by a rinse with isopropanol (Sigma-Aldrich, USA). The fabricated drone was then separated and released from the substrate using a razor blade and transferred to the testing tank using tweezers to be fully immersed in the solution.

Examination of self-recovery in orientation

The restoration time of the microdrone was verified in a water-glycerol mixture with a 5:1 volume ratio (density = 1045.4 kg m⁻³, viscosity = 1.5 Pa s). The microtubes in the

drone automatically trapped air inside as soon as the drone was immersed in the liquid solution. The microdrone was first suspended in the solution with its upright posture, and then a disturbance was introduced by tweezers to put the microdrone into random orientations. The restoration trace from the initial orientation to the upright position was recorded in the time domain using a camera (KP-D20AU, Hitachi, Japan).

3-D swimming

The number and the arrangement of microtubes were determined carefully in order to achieve the desired thrusts and the balanced posture in the equilibrium state. In the 3rd generation drone (Fig. 4), to generate comparable thrusts and similar total volumes of the microbubbles between the sides of lateral 1 and lateral 2, lateral 1 has 2 tubes and lateral 2 has 3 tubes. Note that the lengths of lateral 1 and 2 are different in order to generate yawing. 3 of the 6 vertical tubes are located in the section of lateral 1 and the other 3 tubes in the section of lateral 2. Also note that their arrangement is not symmetric with respect to the y - z plane since lateral 2 is shorter than lateral 1. In order to have 0° pitching as well as 0° rolling angles while in static equilibrium, the 3 vertical tubes in the side of lateral 2 are located at larger x positions than those in the section of lateral 1.

The swimming microdrone was placed in an acrylic tank ($10 \times 10 \times 5 \text{ cm}^3$) filled with either DI water or a water-glycerol mixture (5:1 volume ratio) solution. Two piezoelectric diaphragms (7BB-27-4L0, Murata Electronics, resonance frequency of 4.6 kHz, Japan) were glued to the sidewalls of the tank and connected to a function generator with an amplifier. The frequency to activate each type of microtube was first determined by preliminary frequency-sweeping experiments. A small slab embedded with three tubes of different lengths was fabricated using the Nanoscribe 3-D laser printer. After submerging the slab, the amplitudes of oscillation of each microbubble were recorded while sweeping the frequency from 3 to 15 kHz with an increment of 0.1 kHz but maintaining the voltage amplitude (to the piezo-actuator) constant. The frequency spectrum for each bubble shows multiple peaks. By cross-checking the three frequency spectra, the actuating frequency of each bubble was determined among the peak frequencies, which did not coincide with or was not too close to the peak frequencies in the other two spectra. This selection procedure ensures minimization of the interference or any crosstalk among the actuations of three bubbles. The more detailed procedure is described in ref. 37. The individual activation frequencies of the 3rd generation drone are 5.9 kHz for lateral 1, 7.9 kHz for lateral 2, and 11.7 kHz for vertical. These frequencies deviate from the theoretical prediction (6.9, 10, and 14.5 kHz, respectively) based on the model in ref. 31. This is due to the fact that the bubble oscillation is affected by the entire system setup including the frequency responses of the tank, piezo-actuator, supporting structures,

etc., as studied in previous work.³⁷ The theoretical model may be valid only for bubbles submerged in infinite liquid but does not take into account the effect of the associated components.

For the joint activation, 6.2 kHz is used to generate a forward motion as it induces similar thrusts by both lateral 1 and lateral 2 but keeps propulsion by vertical negligible and requires a single channel amplification. This frequency was also determined experimentally.

Conflicts of interest

There are no conflicts to declare.

Acknowledgements

This work is supported by the National Science Foundation (ECCS-1637815).

References

- 1 M. P. Kummer, J. J. Abbott, B. E. Kratochvil, R. Borer, A. Sengul and B. J. Nelson, *IEEE Trans. Robot.*, 2010, **26**, 1006–1017.
- 2 T. Mirkovic, N. S. Zacharia, G. D. Scholes and G. A. Ozin, *ACS Nano*, 2010, **4**, 1782–1789.
- 3 B. J. Nelson, I. K. Kaliakatsos and J. J. Abbott, *Annu. Rev. Biomed. Eng.*, 2010, **12**, 55–85.
- 4 J. Wu, S. Balasubramanian, D. Kagan, K. M. Manesh, S. Campuzano and J. Wang, *Nat. Commun.*, 2010, **1**, 36.
- 5 D. Patra, S. Sengupta, W. Duan, H. Zhang, R. Pavlick and A. Sen, *Nanoscale*, 2013, **5**, 1273–1283.
- 6 M. Sitti, H. Ceylan, W. Hu, J. Giltinan, M. Turan, S. Yim and E. Diller, *Proc. IEEE Inst. Electr. Electron Eng.*, 2015, **103**, 205–224.
- 7 A. K. Singh and M. Sitti, *Curr. Pharm. Des.*, 2016, **22**, 1418–1428.
- 8 E. M. Purcell, *Am. J. Physiol.*, 1977, **45**, 3–11.
- 9 J. Feng and S. K. Cho, *Micromachines*, 2014, **5**, 97–113.
- 10 G. Hwang, R. Braive, L. Couraud, A. Cavanna, O. Abdelkarim, I. Robert-Philip, A. Beveratos, I. Sagnes, S. Haliyo and S. Régnier, *Int. J. Robot. Res.*, 2011, **30**, 806–819.
- 11 X. Yan, Q. Zhou, J. Yu, T. Xu, Y. Deng, T. Tang, Q. Feng, L. Bian, Y. Zhang, A. Ferreira and L. Zhang, *Adv. Funct. Mater.*, 2015, **25**, 5333–5342.
- 12 A. Barbot, D. Decanini and G. Hwang, *Sci. Rep.*, 2016, **6**, 19041–19048.
- 13 A. M. Maier, C. Weig, P. Oswald, E. Frey, P. Fischer and T. Liedl, *Nano Lett.*, 2016, **16**, 906–910.
- 14 X. Wang, C. Hu, L. Schurz, C. D. Marco, X. Chen, S. Pané and B. J. Nelson, *ACS Nano*, 2018, **12**, 6210–6217.
- 15 U. K. Cheang, D. Roy, J. H. Lee and M. J. Kim, *Appl. Phys. Lett.*, 2010, **97**, 213704.
- 16 E. Steager, C.-B. Kim, J. Patel, S. Bith, C. Naik, L. Reber and M. J. Kim, *Appl. Phys. Lett.*, 2007, **90**, 263901.
- 17 E. B. Steager, M. S. Sakar, D. H. Kim, V. Kumar, G. J. Pappas and M. J. Kim, *J. Micromech. Microeng.*, 2011, **21**, 035001.

- 18 B. J. Williams, S. V. Anand, J. Rajagopalan and M. T. A. Saif, *Nat. Commun.*, 2014, **5**, 3081.
- 19 H. Kim and M. J. Kim, *IEEE Trans. Robot.*, 2015, **32**, 125–137.
- 20 M. M. Stanton, B.-W. Park, A. Miguel-López, X. Ma, M. Sitti and S. Sánchez, *Small*, 2017, **13**, 1603679.
- 21 B.-W. Park, J. Zhuang, O. Yasa and M. Sitti, *ACS Nano*, 2017, **11**, 8910–8923.
- 22 H.-R. Jiang, N. Yoshinaga and M. Sano, *Phys. Rev. Lett.*, 2010, **105**, 268302.
- 23 C. Maggi, F. Saglimbeni, M. Dipalo, F. D. Angelis and R. D. Leonardo, *Nat. Commun.*, 2015, **6**, 7855.
- 24 J. R. Howse, R. A. L. Jones, A. J. Ryan, T. Gough, T. Vafabakhsh and T. Golestanian, *Phys. Rev. Lett.*, 2007, **99**, 48102–48105.
- 25 S. Sundararajan, P. E. Lammert, A. W. Zudans, V. H. Crespi and A. Sen, *Nano Lett.*, 2008, **8**, 1271–1276.
- 26 W. Gao, K. M. Manesh, J. Hua, S. Sattayasamitsathit and J. Wang, *Small*, 2011, **7**, 2047–2051.
- 27 W. Gao, A. Uygun and J. Wang, *J. Am. Chem. Soc.*, 2012, **134**, 897–900.
- 28 W. Gao and J. Wang, *Nanoscale*, 2014, **6**, 10486–10494.
- 29 V. Sridhar, F. Podjaski, J. Kröger, A. Jiménez-Solano, B.-W. Park, B. V. Lotsch and M. Sitti, *Proc. Natl. Acad. Sci. U. S. A.*, 2020, **117**, 24748–24756.
- 30 M. Kaynak, A. Ozcelik, A. Nourhani, P. E. Lammert, V. H. Crespi and T. J. Huang, *Lab Chip*, 2017, **17**, 395–400.
- 31 R. J. Dijkink, J. P. V. D. Dennen, C. D. Ohl and A. Prosperetti, *J. Micromech. Microeng.*, 2006, **16**, 1653–1659.
- 32 J. Feng and S. K. Cho, presented in part at the *IEEE 26th International Conference on Micro Electro Mechanical Systems (MEMS)*, Taipei, Taiwan, 2013.
- 33 J. Feng, J. Yuan and S. K. Cho, *Lab Chip*, 2015, **15**, 1554–1562.
- 34 H. N. Oğuz and A. Prosperetti, *J. Am. Stat. Assoc.*, 1998, **103**, 3301–3308.
- 35 J. Feng and S. K. Cho, presented in part at the *2014 IEEE 27th International Conference on Micro Electro Mechanical Systems (MEMS)*, San Francisco, CA, USA, 2014.
- 36 D. Ahmed, M. Lu, A. Nourhani, P. E. Lammert, Z. Stratton, H. S. Muddana, V. H. Crespi and T. J. Huang, *Sci. Rep.*, 2015, **5**, 9744–9751.
- 37 J. Feng, J. Yuan and S. K. Cho, *Lab Chip*, 2016, **16**, 2317–2325.
- 38 J. F. Louf, N. Bertin, B. Dollet, O. Stephan and P. Marmottant, *Adv. Mater. Interfaces*, 2018, **5**, 1800425.
- 39 L. Ren, N. Nama, J. M. McNeill, F. Soto, Z. Yan, W. Liu, W. Wang, J. Wang and T. E. Mallouk, *Sci. Adv.*, 2019, **5**, eaax3084.
- 40 A. Aghakhani, O. Yasa, P. Wrede and M. Sitti, *Proc. Natl. Acad. Sci. U. S. A.*, 2020, **117**, 3469–3477.
- 41 F.-W. Liu and S. K. Cho, presented in part at the *IEEE 32th International Conference on Micro Electro Mechanical Systems (MEMS)*, Seoul, South Korea, 2019.
- 42 Y.-L. Wang and C.-Y. Lu, *J. Mar. Eng. Technol.*, 2012, **11**, 39–48.
- 43 R. Capocci, G. Dooly, E. Omerdic, J. Coleman, T. Newe and D. Toal, *J. Mar. Sci. Eng.*, 2017, **5**, 13.
- 44 H. Lamb, *Hydrodynamics*, Cambridge University Press, 6th edn, 1932.
- 45 A. A. Shabana, *Theory of vibration: an introduction*, Springer, Cham, 3rd edn, 2019.
- 46 F.-W. Liu, Y. Zhan and S. K. Cho, presented in part at the *IEEE 31th International Conference on Micro Electro Mechanical Systems (MEMS)*, Belfast, Northern Ireland, 2018.
- 47 S. Singhal, C. Moser and M. A. Wheatle, *Langmuir*, 1993, **9**, 2426–2429.
- 48 K. Ferrara, R. Pollard and M. Borden, *Annu. Rev. Biomed. Eng.*, 2007, **9**, 415–477.